Science Advances

AAAS

Supplementary Materials for

Multiple episodes of extensive marine anoxia linked to global warming and continental weathering following the latest Permian mass extinction

Feifei Zhang, Stephen J. Romaniello, Thomas J. Algeo, Kimberly V. Lau, Matthew E. Clapham, Sylvain Richoz, Achim D. Herrmann, Harrison Smith, Micha Horacek, Ariel D. Anbar

The PDF file includes:

Other Supplementary Material for this manuscript includes the following:
(available at advances.sciencemag.org/cgi/content/full/4/4/e1602921/DC1)

Supplementary Information (*SI*) for:

The study section

The Zal section is an open-marine, mainly carbonate succession deposited on a microcontinent in the west-central Tethys Ocean during the Late Permian-Early Triassic (Fig. 1 in the main text). Its geological background has been described in detail by Horacek et al. (*15*), Richoz et al. (*37*), and Leda et al. (*61*). Samples used in this study are from the same sample suites that have been previously analyzed for C isotopes and Sr isotopes by Horacek et al. (*15*), Richoz et al. (*37*), and Sedlacek et al. (*38*). The Zal section is important for several reasons: (1) the study site was isolated from siliciclastic influences and shows limited diagenetic alteration, resulting in preservation of original marine carbonate geochemical signals (*15, 37, 38*); (2) sedimentation was nearly continuous from the Late Permian to the early Middle Triassic, providing a complete record for the Early Triassic; (3) the section was deposited at high sedimentation rates (estimated at ~400 m/Ma), resulting in excellent stratigraphic resolution.

The sampled section starts 37.45 m below the Permian-Triassic boundary (PTB) and extends through 752 m above the PTB. The Upper Permian primarily consists of gray and red nodular limestone. The Griesbachian to the Smithian (0 to 601 m above PTB) is mainly comprised of well-preserved micritic limestone. The Upper Spathian contains mainly dolostone, which persists through the Lower/Middle Triassic boundary.

Horacek et al. (*15*) identified four volcanic dikes in the study section, which are at 50–80 m, 180–190 m, 210–225 m, and 270–300 m above its base. These dikes appear to have had limited influence on geochemical records from Zal, because both the C and Sr isotope profiles at Zal mirror global Early Triassic C and Sr isotope records, even for samples located close to the dikes (*3, 15, 38, 39*). For a detailed description of lithostratigraphy and biostratigraphy, see refs. (*15, 37*).

Evidence for primary seawater δ^{238}U values

Trace elements (e.g., Sr and Mn) substituted into the lattice of carbonate minerals can be used as diagenetic indicators. The incorporation of trace elements into the carbonate lattice is governed by the distribution coefficient, and different types of diagenetic fluids have different trace element compositions. Modern, well-oxygenated seawater is high in Sr relative to Mn such that primary precipitates and early diagenetic phases formed in the presence of seawater are generally enriched in Sr relative to Mn (*62*). This is particularly true for aragonite because of the high distribution coefficient for Sr into aragonite compared to other carbonate minerals (*63*). Early fabric-retentive dolostone can also be enriched in Sr relative to Mn, although dolomite generally has a lower preference for Sr (*64*) and a higher preference for Mn (*65*) compared to calcite.

Meteoric and burial fluids, by contrast, tend to be depleted in Sr relative to seawater (*62*). The recrystallization process also acts to expel Sr from the lattice of carbonate minerals because of its relatively large ionic radius compared to Ca (*66*). As a result, meteoric or burial diagenetic phases are often depleted in Sr relative to precursor marine phases.

Burial fluids can also be substantially enriched in Mn, particularly under reducing conditions (63). This commonly leads to Mn enrichment in burial diagenetic phases. Meteoric fluids are variable in their Mn content—depending largely on redox conditions—such that meteoric calcite phases can be characterized by enrichment or depletion of Mn.

These general relationships have led to the establishment of traditional criteria such as the Mn/Sr ratio to assess the fidelity of primary geochemical signatures in carbonate rocks. For example, Kaufman and Knoll (40) suggested that both limestone and dolostone with Mn/Sr ratios < 10 can be expected to retain their primary carbon isotopic signatures. In this study, we used a conservative Mn/Sr ratio of 2.5 as an initial benchmark for assessing diagenesis.

At Zal, the majority of samples below 500 m yielded Sr concentrations >400 ppm, and most Dienerian-age samples yielded >1000 ppm Sr (fig. S1). These contents are consistent with those reported by Sedlacek et al. (38) and in other studies of marine carbonates interpreted as primary carbonate precipitates. Samples above 500 m have Sr concentrations between 51 ppm and 1070 ppm. The decrease in Sr concentrations at the 500 m of the record corresponds to the appearance of dolomite in the study section.

The Mn/Sr ratios of most samples below 500 m are <0.5 with the exception of the samples below 3.5 m. Samples below 3.5 m have elevated Mn/Sr ratios ranging between 0.1 and 7.5. The majority of the samples above 500 m have Mn/Sr ratios ranging between 0.5 and 4. Because samples below 3.5 m and samples above 500 m have relative higher Mn/Sr ratios than samples between 3.5 and 500 m, samples have been divided into three stratigraphic intervals when evaluating crossplots. Samples with Mn/Sr ratios > 2.5 were not considered further in the analysis and discussion of the study section.

We further looked at crossplots of $\delta^{238}U$–[Sr], $\delta^{238}U$–Mn/Sr, and $\delta^{238}U$–Mg/Ca for all samples as a group as well as samples from below 3.5 m, 3.5-500 m, and above 500 m. No statistically significantly correlations were observed in these crossplots (fig. S2), indicating our $\delta^{238}U$ record is unlikely to have been significantly altered by post-depositional processes including dolomitization.

All of the samples below 3.5 m have Rb/Sr ratios < 0.01, and most of the samples between 3.5 m and 500 m have Rb/Sr ratios < 0.01 (with only 3 outliers > 0.01), indicating minimal incorporation of clays into these carbonates. Samples above 500 m have elevated Rb/Sr ratios ranging between 0.01 and 0.03, indicating potentially larger proportions of clays. However, the lack of covariation between $\delta^{238}U$ and Rb/Sr ratios indicates that the $\delta^{238}U$ profile is unlikely to have been significantly affected by clay contamination (fig. S3).

Changes in the amount of detrital U inputs might also influence bulk carbonate $\delta^{238}U$ values. We examined this possibility by looking at U/Al ratios, which indicate that the U budget in our samples is dominated by authigenic U. The U/Al of most of samples is two to three orders of magnitude higher than the upper continental crust ratio of ~0.331

ppm/wt. % (*67*). Furthermore, there are no statistically significant correlations between U/Al and δ^{238}U (fig. S3), indicating that observed δ^{238}U trends are unlikely related to detrital U inputs.

Because different processes might have altered sample δ^{238}U at different stratigraphic intervals, we therefore provide additional geochemical crossplots (δ^{238}U versus Mn/Sr, Mg/Ca, Rb/Sr, and U/Al) to test whether each of the negative δ^{238}U events were affected by the processes discussed above (figs. S4, S5). No strong statistically significant correlations were observed between δ^{238}U and these proxies, thus further supporting our inference that the negative excursions in the Zal δ^{238}U record have recorded primary seawater events.

The carbon and oxygen isotope correlation for the Zal carbonates (the exact same sample set used for our U isotope study) have been investigated by Horacek et al. (*15*). Briefly, in the Zal section as a whole, there is no correlation between carbon and oxygen isotope values ($R^2 = 0.095$; fig. S6). δ^{13}C and δ^{18}O tend to co-vary if both systems have been influenced by proportional mixing with an external (diagenetic) fluid, and in the case of the Zal section, the lack of co-variation between these parameters is another line of evidence supporting preservation of early, seawater-derived geochemical signatures.

We note that the C1 and C2 δ^{238}U excursions are relatively close to dikes in the Zal section. However, three independent lines of evidence suggest that these dikes had limited influence on our δ^{238}U records. First, samples IZ-13 to IZ-16 are within 10 m of the 50–80 m dike, yet their δ^{238}U values are nearly identical to samples higher and lower in the section. No samples were analyzed close to the 180–190 m dike. Only one sample was analyzed within 10 m of the 210–225 m dike, and that sample (IZ-33) yielded δ^{238}U of −0.31 ‰, which is similar to the next sample above it (IZ-38; −0.34 ‰). Three samples (IZ40-42) were analyzed within 10 m of the 270–300 m sill, and their δ^{238}U values (−0.20 ‰ to −0.41 ‰) are similar to samples from the next 100 m upsection. Second, the C1 δ^{238}U excursion is similar to those observed from other coeval Permian-Triassic boundary sections from a wide range of localities, such as the Dawen, the Dajiang, and the Daxiakou sections in South China, and the Taskent section in Turkey (discussed further below). Third, the δ^{13}C and δ^{238}U excursions of the C1 and C2 cycles are strongly correlated, and since the C1 and C2 δ^{13}C excursions at Zal are known global δ^{13}C excursions of the Early Triassic (*3, 15*), it is logical to infer that the C1 and C2 δ^{238}U excursions were also of global significance.

Finally, we acknowledge the limitations of existing diagenetic proxies for evaluating the diagenesis of carbonate δ^{238}U. The absence of a correlation between various diagenetic tracers and U isotope values does not mean that diagenesis did not occur. Existing indicators of carbonate diagenesis have been primarily developed for carbon, oxygen, and strontium isotopes studies, and further work is required to develop specific diagenetic indicators for uranium isotopes. However, given our present understanding, we argue that the analysis presented above strongly suggests that the Zal section likely recorded primary oceanographic U isotope trend. We further argue that the strongest evidence for the preservation of δ^{238}U in carbonates comes from the independent replications of

secular trends in δ^{238}U in multiple, widely-spaced coeval sections (*25*), and therefore encourage future work to validate that the trends evident in the Zal section can be reproduced in other sections.

Compilation of global carbonate δ^{238}U records for PTB interval

Here we compare our new PTB section (the Zal section in Iran) with four other published PTB sections, the Dawen section (South China) studied by Brennecka et al. (*22*), the Dajiang (South China) and the Taşkent (Turkey) sections studied by Lau et al. (*18*), and the Kamura section (Japan) studied by Zhang et al. (*25*). The paleogeographic locations for these five sections during the latest Permian mass extinction (LPME) are shown in fig. S7, and comparison of δ^{238}U and δ^{13}C records among those sections are shown in fig. S8.

Our Zal record (Fig. 1C and fig. S8) shows persistently high δ^{238}U values in the Upper Permian, with an average of –0.11±0.19 ‰ (2σ). At the PTB interval, a stepped decrease in δ^{238}U results in values as low as –0.69 ‰ by the lowermost Triassic. δ^{238}U values then remain low, varying around –0.50 ‰ through the Griesbachian. The δ^{238}U values of pre- and post-LPME samples are significantly different (*p*<0.01 for a *t*-test).

This observation is consistent with previous δ^{238}U studies (the Dawen section and the Dajiang section in South China, the Taşkent section in Turkey, and the Kamura section in Japan) that show a distinct decrease in δ^{238}U values across the LPME (fig. S8), suggesting that these δ^{238}U trends are primary and record widespread oceanic anoxia during the Permian-Triassic transition. The congruent Permian-Triassic δ^{238}U records at Panthalassic and Tethyan sites confirms that marine δ^{238}U records are globally identical (*25*), and thus supports the use of carbonate U isotopes as a paleoredox proxy for the Early Triassic global ocean.

An additional δ^{238}U study from a South China section by Elrick et al. (*23*) also shows an abrupt negative shift in δ^{238}U of 0.4–0.5 ‰ across the LPME horizon. However, their primary focus was the Middle to Late Permian, and there were only a few data points from the PTB interval, so we have excluded this study in figs. S7 and S8.

At a finer temporal scale, the compilation in fig. S8 shows slight differences in the negative δ^{238}U peaks, i.e., in the peak values and the pattern of overlap among peaks, possibly due to differences in sample distribution and density and uncertainties in age models but perhaps also due to local watermass or diagenetic influences.

The 0.2–0.4 ‰ scatter of δ^{238}U values through the PTB interval may have been due to differential incorporation of ^{238}U-enriched U(IV) from anoxic porewaters during early diagenesis or variation in porewater U-speciation during carbonate recrystallization. Study of modern Bahamian bulk sediments indicates that bank-top carbonates record a normal-distribution of δ^{238}U values ranging from 0.2–0.4 ‰ (average 0.3 ‰) heavier than that of modern seawater (*24*). Measurements of δ^{238}U in deep Bahamian drillcores (Clino, Unda, and IODP Core 1006) extending to the upper Miocene has yielded a similar

normal distribution with a mean and standard deviation of 0.27±0.15 ‰, which is close to the average for bank-top carbonates (Chen et al., in prep.). This offset may reflect differential incorporation of ^{238}U-enriched U(IV) from anoxic porewaters during early diagenesis or variation in porewater U-speciation during carbonate recrystallization (*24, 36*). Porewater data from deep Bahamas drill cores suggests that the extent of burial diagenesis is likely self-limiting because porewater anoxia results in low dissolved U concentrations and renders U essentially immobile (*41*). We therefore conclude that early diagenesis imparts a ~ +0.3 ‰ offset to bulk carbonate δ^{238}U, and that subsequent burial diagenesis likely has no measurable effect. Because of we have found a similar distribution of variation among coeval Permo-Triassic sediments from around the world (fig. S7), we assume that our Zal samples record δ^{238}U approximately 0.3 ‰ heavier than contemporaneous seawater, similar to modern Bahamian carbonate sediments (*24*). Considering the close agreement of δ^{238}U records from multiple, widely-spaced sections across the Permo-Triassic boundary, as well as the similar distribution of δ^{238}U values in modern and ancient carbonate sediments, we argue that the balance of available evidence points to a relatively constant diagenetic offset, both in time and space. Therefore, prior to U isotope mass balance calculations, we applied a diagenetic correction factor of 0.3 ‰ to all measured δ^{238}U values.

Possible timing of onset of oceanic anoxia

We constrained the timing of the onset of oceanic anoxia in the latest Permian by evaluating when the Zal δ^{238}U record began to deviate significantly from pre-crisis background δ^{238}U values. We calculated a LOWESS (LOcally WEighted Scatterplot Smoothing) trend based on the compiled data in fig. S9. A smoothing window of 0.2-Ma was applied, which was optimized based on cross-correlation analysis, to yield the LOWESS trend shown in fig. S9. The negative shift in δ^{238}U began between 252.10 Ma (oldest) and 251.98 Ma (youngest), reflecting an onset that preceded the LPME by at least 40 ka but not more than 160 ka. Although there are some uncertainties in the age models for individual sections, this calculation demonstrates that expansion of oceanic anoxia predated the LPME by a measurable amount. This conclusion is consistent with the findings of several earlier studies that identified the onset of major environmental perturbations up to ~100 ka prior to the latest Permian extinction event (e.g., (*42, 68*).

Age-thickness model for Zal section

An age-thickness model was constructed for the Zal, Iran study section based on six geochronological tie-points, the stratigraphic positions of which in the Zal section were constrained by a combination of conodont biostratigraphic and C-isotope chemostratigraphic data (*15*). The six tie-points include five stage/substage boundaries and one carbon-isotope feature: Latest Permian Mass Extinction (0 m), N2 carbon-isotope peak (30 m), Griesbachian-Dienerian boundary (125 m), Dienerian-Smithian boundary (499 m), Smithian-Spathian boundary (602 m), and Spathian-Anisian boundary (731 m). Due to insufficient biochronological control through conodont or ammonoids biozone and the lack of proper definition of some of these substages an incertitude exists

on the high of these boundaries. The N2 carbon-isotope peak (terminology of Song et al. (14)) is readily identifiable in the Zal carbonate carbon-isotope profile (15).

The time scale used in the present study is that of Algeo et al. (69), which is based on a combination of zircon U-Pb dating studies of the Lower Triassic ($2, 70$-72) and an astrochronological study of the Induan that constrained the relative durations of the Griesbachian and Dienerian substages (73). The ages of the six tie-points in that time scale are: Latest Permian Mass Extinction (251.94 Ma), N2 carbon-isotope peak (251.45 Ma), Griesbachian-Dienerian boundary (251.3), Dienerian-Smithian boundary (251.0 Ma), Smithian-Spathian boundary (250.6 Ma), and Spathian-Anisian boundary (247.2 Ma).

The age-thickness model for the Zal section is shown in fig. S1. The model shows moderate sedimentation rates in the late Changhsingian to mid-Griesbachian (60-90 m Ma^{-1}), accelerating during the late Griesbachian (620 m Ma^{-1}) and Dienerian (1250 m Ma^{-1}), and then declining during the Smithian (260 m Ma^{-1}) and Spathian (70 m Ma^{-1}). Other age models (Ogg, 2012) lead to lower but still significantly elevated peak sedimentation rates (435 m Ma^{-1} in the Dienerian) and have the disadvantage of yielding erratic changes from one substage to the next, as opposed to the smooth pattern of acceleration and deceleration yielded by our age model (fig. S10). The exceedingly high sedimentation rates associated with the Dienerian in all age models must reflect a major episode of tectonic subsidence of the Iranian microcontinent during that substage of the Early Triassic.

Cross-correlation analysis

The carbon, uranium, and strontium isotope profiles for the Zal, Iran study section (Fig. 1 in the main text) were compared using cross-correlation analysis (74) for the purpose of establishing relative lead/lag relationships among these records. The underlying principle of cross-correlation analysis is that two records are offset relative to each other in successively larger increments, and the degree of correspondence is evaluated at each step. The metric that we used to evaluate the degree of correspondence between pair-wise records was Pearson's correlation coefficient (r).

Cross-correlation analysis requires that data series be spaced at equal intervals of length or time in order to be able to offset one record relative to another at equal increments. Thus, although all three of the Zal isotopic records were generated from the same suite of samples, it was nonetheless necessary to resample each record to produce data series at equal intervals. We chose to resample the Zal dataset at equal intervals of time (rather than length) based on the ages for individual samples calculated from our age-thickness model (see above). These ages were used to generate a LOWESS curve for each isotopic profile (Fig. 1) with estimated values at 25-ka nodes between about 252.25 Ma and 249.75 Ma (the exact interval depended on the age range of the specific isotopic record).

The LOWESS records were cross-correlated in a pairwise manner: $\delta^{238}U$-vs- $\delta^{13}C$ and $^{87}Sr/^{86}Sr$-vs- $\delta^{13}C$. The C-isotope profile is longer, more complete (i.e., fewer gaps), and more coherent (i.e., less sample-to-sample variance) than the U- and Sr-isotope profiles,

so it was chosen as the base record for cross-correlation analysis. For each pair of records, one was offset relative to the other in increments of 25 ka, with a correlation coefficient calculated at each step. We conducted cross-correlation analysis based on (1) the full (~2.5-Ma-long) isotopic records, and (2) windowed intervals of each record (where correlation coefficients were calculated based on 200-ka data windows). Analysis of the full records demonstrated that quantifiable lead/lag relationships existed, and analysis of shorter data windows demonstrated that the lead/lag relationships changed with time.

The correlations between δ^{238}U and δ^{13}C are strongly positive (mostly r > +0.6) throughout the Early Triassic study interval (fig. S11–top), demonstrating significant direct covariation among these two proxies. The δ^{238}U record lagged the δ^{13}C record mostly by 75-175 ka (mean ~125 ka) during the Griesbachian to Smithian, but this lag went to zero during the Spathian, mainly because of lack of variation in the δ^{238}U and δ^{13}C records during that substage. The observation that the δ^{238}U record lagged the δ^{13}C record is a reflection of the longer residence time of U in seawater (~320-560 ka; (75)) than that of dissolved inorganic carbon (DIC) (~100 ka; (76)) and, hence, the slower response time of the U-isotope system to global perturbations.

The correlations between ^{87}Sr/^{86}Sr and δ^{13}C are strongly negative (mostly r < −0.5) throughout the Early Triassic study interval (fig. S11–bottom), demonstrating significant inverse covariation among these two proxies. The ^{87}Sr/^{86}Sr record led the δ^{13}C record by intervals mostly ranging from 0 to 225 ka (mean ~100 ka) during the Griesbachian to Smithian, but this lag reversed during the Spathian, when δ^{13}C led ^{87}Sr/^{86}Sr by ~75 ka. Strontium has a longer residence time in modern seawater (~2 Ma; Davis et al., 2003) than dissolved inorganic carbon, and this is unlikely to have varied much in the Early Triassic given that the largest source of Sr to seawater is continental weathering. Thus, the observation that Sr-isotopic variation led C-isotopic variation is most easily interpreted as the result of continental weathering fluxes driving changes in the Early Triassic marine system. This is consonant with substantial evidence for major increases in terrestrial fluxes to marine systems during the Early Triassic (e.g., (46, 77). The observation of a reversal in lead/lag relationships close to the Smithian-Spathian boundary (i.e., a shift to δ^{13}C leading ^{87}Sr/^{86}Sr) suggests that this continental driver of Early Triassic marine environmental changes tapered off or terminated around that time.

High-resolution intercomparison of Zal δ^{13}C, ^{87}Sr/^{86}Sr, and δ^{238}U records

The relationship of the Zal δ^{238}U profile to previously published δ^{13}C and ^{87}Sr/^{86}Sr profiles for the same sample suite was investigated by generating a LOWESS curve for each record (Fig. 2 in the main text). Each of these records exhibits three cycles of variation through the Griesbachian-Smithian substages of the Early Triassic. The C-isotope minima and maxima were previously labeled N1-N3 ("negative" excursions) and P1-P3 ("positive" excursions), respectively, by Song et al. (14, 78). In this manuscript, we labeled the covariation in C-Sr-U isotope systems using C1 to C4, which donate four different cycles (Fig. 2 in the main text).

The first cycle (**C1**), which commenced at the LPME horizon and ended around the Griesbachian-Dienerian boundary, was characterized by (i) an initially rapid negative shift in $\delta^{238}U$ that slowed before reaching a minimum in the middle-to-late Griesbachian, (ii) an initially rapid negative shift in $\delta^{13}C$ that peaked in the early Griesbachian before a positive rebound in the late Griesbachian, and (iii) a sharp rise in $^{87}Sr/^{86}Sr$ in the early Griesbachian followed by little change.

The second cycle (**C2**), which commenced around the Griesbachian-Dienerian boundary and ended around the Dienerian-Smithian boundary, was characterized by (i) a large negative shift in $\delta^{238}U$ to a minimum in the mid-Dienerian, (ii) a relatively small negative C-isotope shift with a peak in the early Dienerian that was followed by a large positive shift culminating at the Dienerian-Smithian boundary, and (iii) a long, steady rise in $^{87}Sr/^{86}Sr$ through most of the Dienerian.

The third cycle (**C3**), which commenced around the Dienerian-Smithian boundary and ended in the earliest Spathian, was characterized by (i) a relatively small negative shift in $\delta^{238}U$ with a minimum in the late Smithian, (ii) a large negative C-isotope shift with a minimum also in the late Smithian, and (iii) relatively uniform $^{87}Sr/^{86}Sr$ through most of the Smithian followed by a sharp rise in the late Smithian. The 3rd pair of negative excursions in $\delta^{238}U$ and $\delta^{13}C$ appears synchronous. However, there are several considerations here: (1) the U peak is effectively defined by a single point, so it is not very secure; and (2) there is either an unconformity or a highly condensed interval at the Smithian-Spathian boundary (SSB) in the Zal section. The unconformity/condensed interval may be reflected in the shape of the $\delta^{13}C$ curve—in most Lower Triassic sections, the $\delta^{13}C$ minimum is mid-Smithian (e.g., Song et al. (*14*)), but at Zal it appears at the very top of the Smithian interval, which suggests that the upper Smithian may be missing. The cause of this unconformity may have been strong cooling at the SSB, leading to renewed continental icesheet growth and a modest sea-level fall that affected shallow-water but not deep-water sections.

The Spathian may represent a fourth cycle (**C4**) similar to the preceding three cycles in that both the $\delta^{238}U$ and $\delta^{13}C$ profiles exhibit a long-term, gradual shift to another minimum in the latest Spathian ($\delta^{13}C$) or at the Spathian-Anisian boundary ($\delta^{238}U$), although the $^{87}Sr/^{86}Sr$ record lacks sufficient detail in the Spathian for comparison to the other records (Fig. 2 in the main text).

Estimation of weathering rates and seawater PO_4^{3-} levels in the Early Triassic ocean

We constructed a simple box model to calculate seawater PO_4^{3-} concentrations in the Early Triassic ocean for the purpose of exploring possible connections between seawater nutrient levels and expanded oceanic anoxia. The model was constructed in three parts, first using Sr isotopes to constrain Early Triassic weathering rates, then using these rates to estimate PO_4^{3-} fluxes to seawater, and finally combining this source estimate with estimated sinks to calculate the PO_4^{3-} concentration through time.

To determine Early Triassic weathering rates, which largely control riverine PO_4^{3-} fluxes, we first constructed a Sr isotope budget for the Early Triassic following Sedlacek et al. (38). We constructed a smoothed Early Triassic $^{87}Sr/^{86}Sr$ record for this purpose by using a recently published Sr isotope data from Zal (38) and using LOWESS smoothing and piecewise cubic interpolation to generate a continuous $^{87}Sr/^{86}Sr$ record (fig. S12A; green curve). We then developed a forward model to calculate seawater $^{87}Sr/^{86}Sr$ through time (fig. S12A; red curve), and varied the riverine Sr flux to match the smoothed $^{87}Sr/^{86}Sr$ record.

The three principal sources of Sr to seawater are rivers (i.e., continental crust), weathering of ocean crust/hydrothermal, and diagenesis of marine carbonates (38, 79). Seawater $^{87}Sr/^{86}Sr$ is influenced most strongly by (1) the Sr isotopic composition of the riverine flux (~0.712 in the modern), and (2) the ratio of the riverine to hydrothermal fluxes (1.65, based on estimated baseline fluxes of ~3.3 and 2.0×10^{10} mol yr^{-1}, respectively) (38, 80).

Changes to seawater $^{87}Sr/^{86}Sr$ can be described by differential mass balance equations for the seawater Sr inventory and $^{87}Sr/^{86}Sr$ ratio, respectively

$$\frac{dSr}{dt} = J_{river}^{Sr} + J_H + J_{DC} - \frac{1}{\tau_{Sr}} \cdot Sr \tag{1}$$

$$\frac{d(Sr \cdot \frac{^{87}Sr}{^{86}Sr})}{dt} = J_{river}^{Sr} \cdot (\frac{^{87}Sr}{^{86}Sr})_{river} + J_H \cdot (\frac{^{87}Sr}{^{86}Sr})_H + J_{DC} \cdot (\frac{^{87}Sr}{^{86}Sr})_{DC} - \frac{1}{\tau_{Sr}} \cdot Sr \cdot (\frac{^{87}Sr}{^{86}Sr}) \tag{2}$$

where Sr is the Sr inventory in the ocean, J_{river}^{Sr}, J_H, and J_{DC} are the total amount of Sr supplied by rivers, ocean crustal hydrothermal activity, and marine diagenetic carbonates, respectively. $(^{87}Sr/^{86}Sr)_{river}$, $(^{87}Sr/^{86}Sr)_H$, and $(^{87}Sr/^{86}Sr)_{DC}$ are the $^{87}Sr/^{86}Sr$ ratio for rivers, ocean crustal hydrothermal, and marine diagenetic carbonates, respectively, and τ_{Sr} is the residence time of Sr in the ocean. Model parameterization was based on studies of the modern and ancient marine Sr cycle and are summarized in table S1.

Equation (2) can be simplified by using the product rule to expand the left-hand side and substituting in equation (1) to get to an expression for the change in the isotope ratio itself

$$\frac{d(\frac{^{87}Sr}{^{86}Sr})}{dt} = \frac{J_{river}^{Sr} \cdot (\frac{^{87}Sr}{^{86}Sr})_{river} + J_H \cdot (\frac{^{87}Sr}{^{86}Sr})_H + J_{DC} \cdot (\frac{^{87}Sr}{^{86}Sr})_{DC}}{Sr} - \frac{J_{river}^{Sr} + J_H + J_{DC}}{Sr} \cdot (\frac{^{87}Sr}{^{86}Sr}) \tag{3}$$

We further define a factor, R

$$R = \frac{J_{river}^{Sr}}{J_{modern}} \tag{4}$$

which scales the Early Triassic riverine Sr flux, J_{river}^{Sr}, relative to the Sr flux in modern rivers, J_{modern}.

In our model, we make use of a simplified approach in which the fluxes and isotopic compositions for the hydrothermal and diagenetic carbonate sources are assumed to be invariant: (1) 2.0×10^{10} moles/yr and 0.7030 $^{87}Sr/^{86}Sr$ for the hydrothermal flux, and (2) 0.3×10^{10} moles/yr and 0.7084 $^{87}Sr/^{86}Sr$ for the diagenetic carbonate flux. Similar to Sedlacek et al. (38), we also adopted a higher value for the hydrothermal flux (2.0×10^{10} moles/yr) than in the modern (1.0×10^{10} moles/yr) owing to generally higher eustatic sea level and, thus, inferred higher ocean-crustal spreading rates in the Late Paleozoic (see justification by Sedlacek et al. (38)).

We used a $(^{87}Sr/^{86}Sr)_{river}$ of 0.7090 for the first 0.5 Ma of the model simulation based on the assumption that the riverine flux likely contained large amounts of Sr derived from weathering of Siberian Traps basalts (43) for an interval up to ~0.5 Ma following the eruption events (81, 82). Thereafter, $(^{87}Sr/^{86}Sr)_{river}$ was set to 0.7120, which is an average value for modern rivers (83). The $(^{87}Sr/^{86}Sr)_{river}$ model input record is shown in fig. S12B. Initial conditions for the model were calculated to assuming a steady state Sr cycle in the Late Permian, with a seawater $^{87}Sr/^{86}Sr = 0.7071$, corresponding to measured values in the Late Permian ocean (38). Equations 1 and 3 were solved as a coupled system of differential equations using simple first-order Euler integration. We optimized the resulting model output by using non-linear fitting to adjust the river Sr flux, reflected in the R parameter, in order to achieve the best fit to the observed seawater $^{87}Sr/^{86}Sr$ isotope record (fig. S12A; red curve). The resulting estimates suggest the Early Triassic riverine Sr fluxes were general ~2-4 × higher than present day and briefly higher than 7 × (fig. S12C) in agreement with previously published results (38).

The riverine PO_4^{3-} flux was estimated based on estimated riverine Sr flux by

$$J_{river}^{P} = R \cdot J_{river}^{Sr} \cdot \left(P/Sr\right)_{river} \tag{5}$$

where $(P/Sr)_{river}$ is the P/Sr ratio of modern rivers. The major sources of P and Sr to the ocean is weathering release of P and Sr from the upper continental crust and transport of dissolved/particulate P and Sr to the oceans via rivers (50, 84-86). The modern reactive P flux to the oceans, sourced primarily by rivers, is estimated to be approximately (2–3) × 10^{11} mol yr^{-1} (87, 88). The vast majority of P in rivers is present as a solid phase; according to most estimates ~90% of the P delivered by rivers to the ocean is in particulate form (84, 89). About 99% of particulate P are removed from seawater at the coastal zones (84). Thus, the net riverine P flux (the total amount of P that can pass the coastal zone and dissolve in seawater) to the ocean is estimated to be 2–3×10^{10} mol yr^{-1}. The riverine Sr flux to the ocean is estimated to be 3.3×10^{10} mol yr^{-1} (79). The estimated P/Sr ratio (moles/moles) therefore ranges from 0.61 to 0.91. In the Fig. 3C of the main text, we have presented modeling output using a P:Sr ratio of both 0.61 and 0.91, respectively, to test the modeling sensitivities associated with the P:Sr ratio.

Because the riverine flux represents the main phosphorus source to the ocean (50, 84-86), we can then model the seawater PO_4^{3-} concentration using a simple mass balance model

$$\frac{d\left[PO_4^{3-}\right]}{dt} = \frac{J_{river}^{P}}{V_{Ocean}} - \frac{\left[PO_4^{3-}\right]}{\tau_{PO_4}} \tag{6}$$

where $[PO_4^{3-}]$ is the seawater phosphate concentration, J_{river}^P is the riverine PO_4^{3-} flux, V_{ocean} is the volume of the ocean, and τ_{PO4} is the residence time of PO_4^{3-} in the ocean.

The seawater residence time of PO_4^{3-} is thought to be depend significantly on average ocean redox conditions because the presence of iron oxides at the seawater-sediment interface inhibits diffusion of porewater PO_4^{3-} back to the water column, enhancing PO_4^{3-} burial efficiency (50, 86, 90-92). To capture this behavior in our simplified model, we assume the residence time of PO_4^{3-} and the anoxic seafloor area follows a sigmoidal relationship in which τ_{PO4} increases when anoxic seafloor area expands, an assumption that has been applied in previous modeling studies (50, 52, 90). In the sigmoidal curve, the two endmembers are $\tau_{PO4} = 69$ ka when $\delta^{238}U = -0.4$ ‰, and $\tau_{PO4} = 4\times69$ ka when $\delta^{238}U = -1.0$ ‰.

Equation 6 was integrated using first-order Euler integration with an initial $[PO_4^{3-}]$ concentration of 0.610 uM (when P:Sr ratio = 0.61) and 0.736 (when P:Sr ratio = 0.91), calculated assuming the Late Permian ocean was at steady state. The resulting PO_4^{3-} concentrations are shown in figure S12D. PO_4^{3-} concentrations peaked at ~251.6 Ma, ~251.2–250.9 Ma, 250.6 Ma, and 247.3 Ma, which generally correlate to peaks in anoxia seafloor areas calculated from the U isotope model (Fig. 3 in the main text).

table S1. Strontium and phosphorus model parameterization.

Parameter	Value	Reference
Sr	1.25×10^{17} moles	Richter and Turekian (79)
J_{river}^{Sr}	3.3×10^{10} moles/yr	Richter and Turekian (79)
J_H	2×10^{10} moles/yr	Richter and Turekian (79); Sedlacek et a. (38)
J_{DC}	0.3×10^{10} moles/yr	Richter and Turekian (79)
$(^{87}Sr/^{86}Sr)_{river}$	0.7090, 0.7210	Palmer and Edmond (83), and see adjusting above
$(^{87}Sr/^{86}Sr)_H$	0.7030	Albarède et al. (93)
$(^{87}Sr/^{86}Sr)_{DC}$	0.7084	Richter and Liang (94)
τ_{Sr}	3×10^6 yr	Hodell et al. (95)
J_{river}^P	2×10^{11} moles/yr	Tyrrell (88)
$(P/Sr)_{ratio}$	0.61–0.91 moles/moles	Calculated using modern riverine fluxes
τ_{PO4}	Follows a sigmoidal relationship with anoxic seafloor area	Payne an Kump (52); Ingall and Jahnke (90); Van Cappellen, E. D. Ingall (50)
V_{ocean}	1.34×10^{21} L	

Box model estimates for f_{anox}

The implied changes to the extent of bottom water anoxia can be described by differential mass balance equations for the seawater uranium inventory and its isotopic composition, respectively (following Lau et al. (18))

$$\frac{dN_{sw}}{dt} = J_{riv}^U - J_{oxic} - J_{anox}$$

(7)

$$\frac{d(N_{sw} \cdot \delta^{238}U_{sw})}{dt} = J_{riv}^{U} \cdot \delta^{238}U_{sw} - J_{oxic} \cdot \delta^{238}U_{oxic} - J_{oxic} \cdot \delta^{238}U_{anox} \tag{8}$$

$$\delta^{238}U_{anox} = \delta^{238}U_{sw} + \Delta_{anox} \tag{9}$$

$$\delta^{238}U_{oxic} = \delta^{238}U_{sw} + \Delta_{oxic} \tag{10}$$

As with Eq. 2, Eq. 8 can be simplified to give an expression for the changing isotope composition

$$\frac{d(\delta^{238}U_{sw})}{dt} = \frac{J_{riv}^{U} \cdot (\delta^{238}U_{riv} - \delta^{238}U_{sw}) - J_{oxic} \cdot \Delta_{oxic} - J_{anox} \cdot \Delta_{anox}}{N_{sw}} \tag{11}$$

where N_{sw} is the oceanic uranium inventory in moles, $\delta^{238}U_{sw}$ is the value of seawater, $\delta^{238}U_{riv}$ is the value of the riverine source, $\delta^{238}U_{anox}$ is the U isotope composition of anoxic sedimentary sinks, and $\delta^{238}U_{oxic}$ is average U isotope compositions of the remaining other sinks. Here, we simplify the inputs to J_{riv}^{U}, the riverine flux, whose modern value is ~4×10^{7} moles U/yr (29). The outputs are assumed to consist of the anoxic sediment sink (J_{anox}) and the sum of the other sinks (J_{oxic}). In this model, we use the estimate of 0.6×10^{7} moles U/yr (31) for J_{anox} and calculate J_{oxic} by mass balance to an initial steady-state value of 3.4×10^{7} moles U/yr. $\Delta_{anox} = +0.6$ ‰ is the effective fractionation factor associated with anoxic sediment deposition (96), and Δ_{oxic} is the effective fractionation factor associated with the remaining other sinks (+0.005 ‰, calculated to maintain isotopic steady state in the modern ocean (e.g, Brennecka et al. (22), Montoya-Pino et al. (97), and Wang et al. (98)).

We define the oxic and anoxic sinks in Eq. 7–11 assuming a first-order dependence on seawater U concentration

$$J_{anox} = k_{anox} \cdot N_{sw} \cdot A_{anox} \tag{12}$$

$$J_{oxic} = k_{oxic} \cdot N_{sw} \cdot A_{oxic} \tag{13}$$

where A_{anox} and A_{oxic} are the total seafloor area overlain by anoxia waters and the total seafloor area overlain by non-anoxic waters, respectively, and k_{anox} and k_{other} are rate constants associated with anoxic sediment deposition and all other sediment deposition and are calculated for the modern uranium system (e.g., Wang et al. (98) and Lau et al. (18)).

We further define the fraction of anoxic seafloor area overlain by anoxic water

$$f_{anox} = \frac{A_{anox}}{A_{ocean}} \tag{14}$$

where f_{anox} is the total seafloor area overlain by anoxic waters, and A_{ocean} is the total seafloor area of modern ocean.

Equations 7 and 11 were solved using the same numerical method used for the Sr isotope model presented above. In order to drive the model, we adjusted the fraction of anoxic seafloor (f_{anox}) to optimize the fit between the model and measured U isotope composition. The modeling outputs of f_{anox} have been summarized in Fig. 3 B of the main text. In Fig. 3 B, we have presented modeling output without and with a diagenetic offset of 0.3 ‰,

respectively, to consider uncertainties associated with the diagenetic offset between Early Triassic carbonates and Early Triassic seawater. Model parameterization was based on studies of the modern U cycle and are summarized in table S2.

table S2. Uranium box model parameterization.

Parameter	Value	Reference
$N_{sw,0}$	1.96×10^{13} mol U	Ku et al. (*26*)
J_{riv}^{U}	4×10^{7} mol U yr^{-1}	Morford and Emerson (*31*)
J_{anox}	0.6×10^{7} mol U yr^{-1}	Morford and Emerson (*31*)
J_{oxic}	3.4×10^{7} mol U yr^{-1}	Calculated at steady state conditions
$\delta^{238}U_{river}$	–0.26 ‰	Andersen et al. (*30*)
$\delta^{238}U_{seawater}$	–0.39 ‰	Tissot and Dauphas (*29*)
Δ_{anox}	+0.6 ‰	Andersen et al. (*96*)
Δ_{oxic}	+0.005 ‰	Calculated at steady state conditions
k_{anox}	1.41×10^{-19} yr^{-1} m^{-2}	Calculated using modern parameters with equation (*14*)
k_{oxic}	4.82×10^{-21} yr^{-1} m^{-2}	Calculated using modern parameters with equation (*13*)
A_{ocean}	3.62×10^{14} m^{2}	Lutgens, Frederick. Essentials of Geology. New York: MacMillan, 1992: 269.
V_{ocean}	1.34×10^{21} L	"The World Ocean." The Columbia Encyclopedia. CD-ROM. 2007, 6th Ed. New York: Columbia University Press.
Diag. corr. factor	0.3 ‰	Romaniello et al. (*24*)

Patterns of marine invertebrate clade recovery following the LPME

Patterns of recovery of marine invertebrate clades following the latest Permian mass extinction have been reviewed by Wei et al. (*4*) and Chen and Benton (*1*). Below is a brief summary:

Conodonts and ammonoids: these clades rebounded rapidly from the end-Permian mass extinction, but they suffered biodiversity losses at the ends of the Griesbachian, Smithian, and Spathian substages of the Early Triassic (*5, 6, 99*).

Foraminifers, brachiopods, and ostracods: a sustained diversity increase began in the early Smithian (early Olenekian) (*9*) and accelerated during the Anisian (early Middle Triassic) (*8*).

Gastropods: a sustained diversity increase began in the early Smithian (early Olenekian) (*9*) and accelerated during the Anisian (early Middle Triassic) (*8*). The sizes of gastropod and bivalve shells were reduced across the P–Tr boundary and during the Griesbachian but returned to pre-extinction dimensions by the Anisian (*100-102*).

Trace-makers: they decreased during the LPME and recovered slowly in the Early Triassic (*7, 103*). Small trace-fossil burrow size, low tiering levels, and low ichnofabric indices (bioturbation) generally persisted until the end of the Smithian substage. The early Spathian is marked by a strong increase in trace-fossil diversity and complexity (*7, 103*).

Reef-builders: they display a "reef gap", as represented by the absence of heavily calcified corals, that persisted through the Early Triassic (*4, 104*).

Ammonoid extinction rates

Data and methods

We evaluated ammonoid extinction rates at a high level of stratigraphic resolution (finer than substage) through the Early Triassic for the purpose of comparing biodiversity patterns with the detailed records of $\delta^{238}U$, $\delta^{13}C$, and $^{87}Sr/^{86}Sr$ from the Zal study section. We derived ammonoid range data from the Paleobiology Database (www.paleobiodb.org), which was accessed using the PaleoDB API. We supplemented those occurrences with Dienerian family ranges from the northern Indian margin from Ware et al. (*105*), as the underlying occurrences for that dataset have not yet been published and cannot be included in the Paleobiology Database. We calculated extinction rates at the taxonomic family level because many genera are confined to a single biozone even with the high-resolution data available. Extinction rates were calculated using the boundary-crosser method (*106*), and some time intervals had sparse occurrences, preventing us from using other methods such as the three-timer extinction rate (*107*). We calculated extinction rates separately within three regions: the northern Indian margin, the western United States, and the Boreal realm (Canadian Arctic and Russian Arctic). Inter-regional correlations have been developed for some time intervals (such as the Smithian tropics (*107*)) but are not available for the entire Early Triassic, so we were unable to produce a single multi-regional dataset. All extinction rates were calculated at a temporal resolution finer than substage; some intervals are formally defined biozones, whereas others are local/regional "horizons" or "beds." We also calculated a global extinction rate for ammonoid families at the Late Permian mass extinction horizon. This rate was calculated at the stage level, using Wuchiapingian, Changhsingian, and Early Triassic data from the Paleobiology Database.

Ammonoid zonal correlations

In the Griesbachian, the only published data with finer-than-substage resolution comes from the Boreal realm. We used the zonal correlations of Tozer (*108*) and Ermakova (*109*) and assumed equal durations for each of the three zones. The base of the lowest zone (*Otoceras concavum*) may overlap with the terminal Changhsingian in the paleoequatorial regions, but should be entirely post-extinction.

Dienerian data from the northern Indian margin were binned into the 12 Unitary Association zones of Ware et al. (*105*), which we assumed to have equal duration. We also scaled the three Boreal zones to have equal duration, although we compressed the final interval (*Vavilovites sverdrupi/V. turgidus/Kingites korostelevi* Zone) to accommodate the observation that the overlying *hedenstroemi* Zone may be upper Dienerian at its base (*110*). Implied correlations within the Dienerian in fig. S13 are only approximate, although it seems plausible that the *Vavilovites meridialis* and *Kingites davidsonianus* beds of the northern Indian margin may be correlative to the *Vavilovites sverdrupi*, *V. turgidus*, and *Kingites korostelevi* zones in the Boreal region.

Brühwiler et al. (*111*) defined 13 Unitary Association zones for the Smithian succession of the northern Indian margin. We scaled those intervals to be of equal duration and used the scheme of Brayard et al. (*107*) to correlate ammonoid zones from the western USA (*107*) and Boreal region (*108, 109*). Unlike in the Dienerian or Spathian, the inter-regional correlations are robust, particularly between the two paleoequatorial regions (Indian margin, western USA).

The Spathian timescale is based on the ammonoid zonation (including informal beds) developed for the western USA by Guex et al. (*112*). We correlated the carbon isotope curve to Spathian ammonoid zonation by aligning the inflection point at the most negative Spathian carbon isotope values with the lower-middle Spathian boundary (above the *Procolumbites* beds) following Galfetti et al. (*72*). The Zal carbon isotope curve implies that the middle and upper Spathian, as defined by ammonoids, may be very thin at this location. We scaled the three early Spathian intervals to have equal duration, and did the same for the four middle and late Spathian zones. We scaled the seven intervals to have equal duration. The Boreal region has been subdivided into four successive intervals (*109*), which we correlated tentatively to the more finely-resolved western USA scale. Implied correlations within the Spathian in fig. S13 are only approximate.

We include data from the lower and part of the middle Anisian from the western USA and the Boreal realm. The western USA zonation is based on Bucher (*113*) and is correlated approximately to Boreal zonations. Again, we scale the four western USA levels to have equal duration.

Extinction rate results

Boreal data may suggest a mid-Griesbachian extinction peak (*Otoceras boreale* Zone), although the boundary-crosser value is only slightly elevated. However, there are only a few boundary-crossing families in this interval, soon after the LPME, so it is mathematically impossible to obtain high absolute extinction rates. This turnover, which marks a transition from dominant Otoceratidae to dominant Ophiceratidae, is likely an important event.

Ammonoids suffered elevated family extinction rates around the middle-late Dienerian transition on the northern Indian margin (*Ambites bjerageri/Ambites lilangensis* beds and *Vavilovites meridialis* beds of Ware et al. (*105*)). In the Boreal region, the extinction in the *Vavilovites sverdrupi/V. turgidus/Kingites korostelevi* Zone is slightly later, within the late Dienerian, in our correlation scheme. However, correlations in this interval are tentative so it is possible that the two extinctions were synchronous. At this point, it is not possible to determine whether extinctions near the middle-late Dienerian transition were synchronous or slightly diachronous.

All three regions exhibit a pronounced and synchronous extinction peak at the end of the middle Smithian (*Nyalamites angustecostatus* beds along the northern Indian margin, Owenites beds/*Meekoceras gracilitatis* Zone in the western USA, and *Euflemingites romunderi/Lepiskites kolymensis* Zone in the Boreal region). On the northern Indian

margin, extinction rates are also elevated in the preceding interval (*Pseudoceltites multiplicatus* beds); this either indicates that the extinction spanned both intervals in the late middle Smithian or that the earlier extinctions are biased by the Signor-Lipps effect.

Boreal ammonoids apparently underwent a major extinction in the latest Spathian (*Keyserlingites subrobustus*/*Olenikites spiniplicatus* Zone), although the western USA data do not show a comparable peak. Instead, extinction rates in the western USA were slightly elevated for several intervals leading up to the Spathian/Anisian boundary. Mid-late Spathian data are sparse in the western USA, so it seems reasonable to interpret the prolonged episode of slightly elevated rates as arising from the Signor-Lipps effect in the boundary-crosser data, which would be consistent with a larger extinction near the Spathian/Anisian boundary. It is also possible that the Boreal losses were a regional phenomenon that was more intense than extinctions elsewhere.
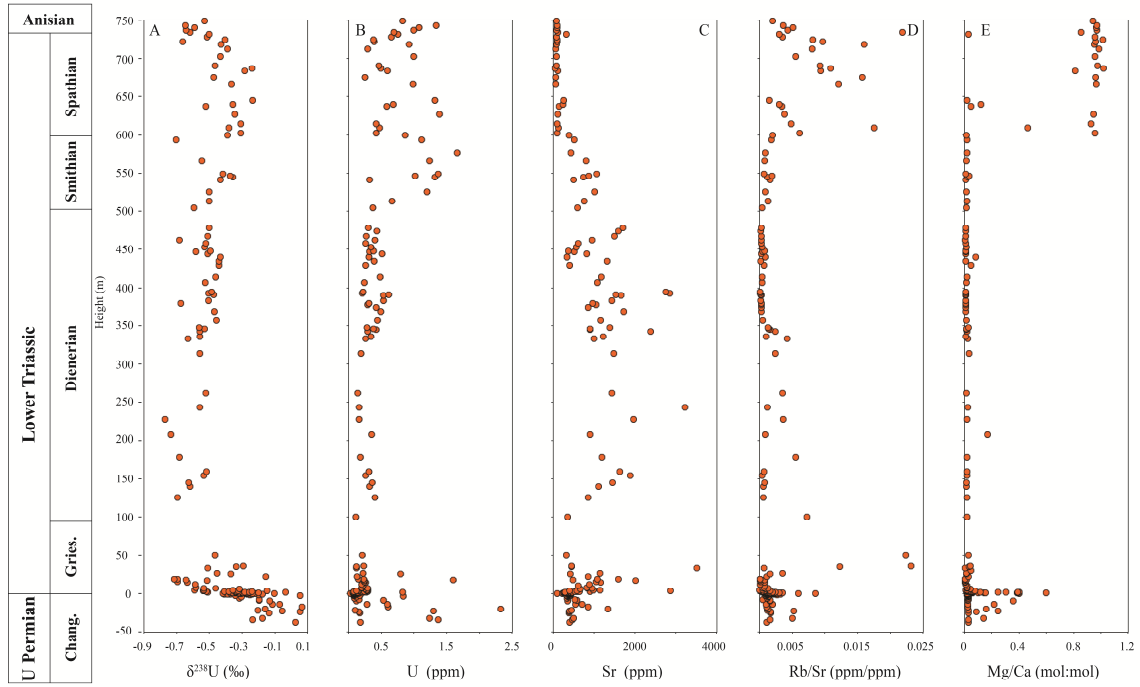
fig. S1. Geochemical profile of Zal, Iran. (**A**) δ^{238}U profile, (**B**) U concentration profile, (**C**) Sr concentration profile, (**D**) Rb/Sr ratio profile, and (**E**) Mg/Ca (mol:mol) profile. Chang.: Changhsingian; Gries.: Griesbachian.
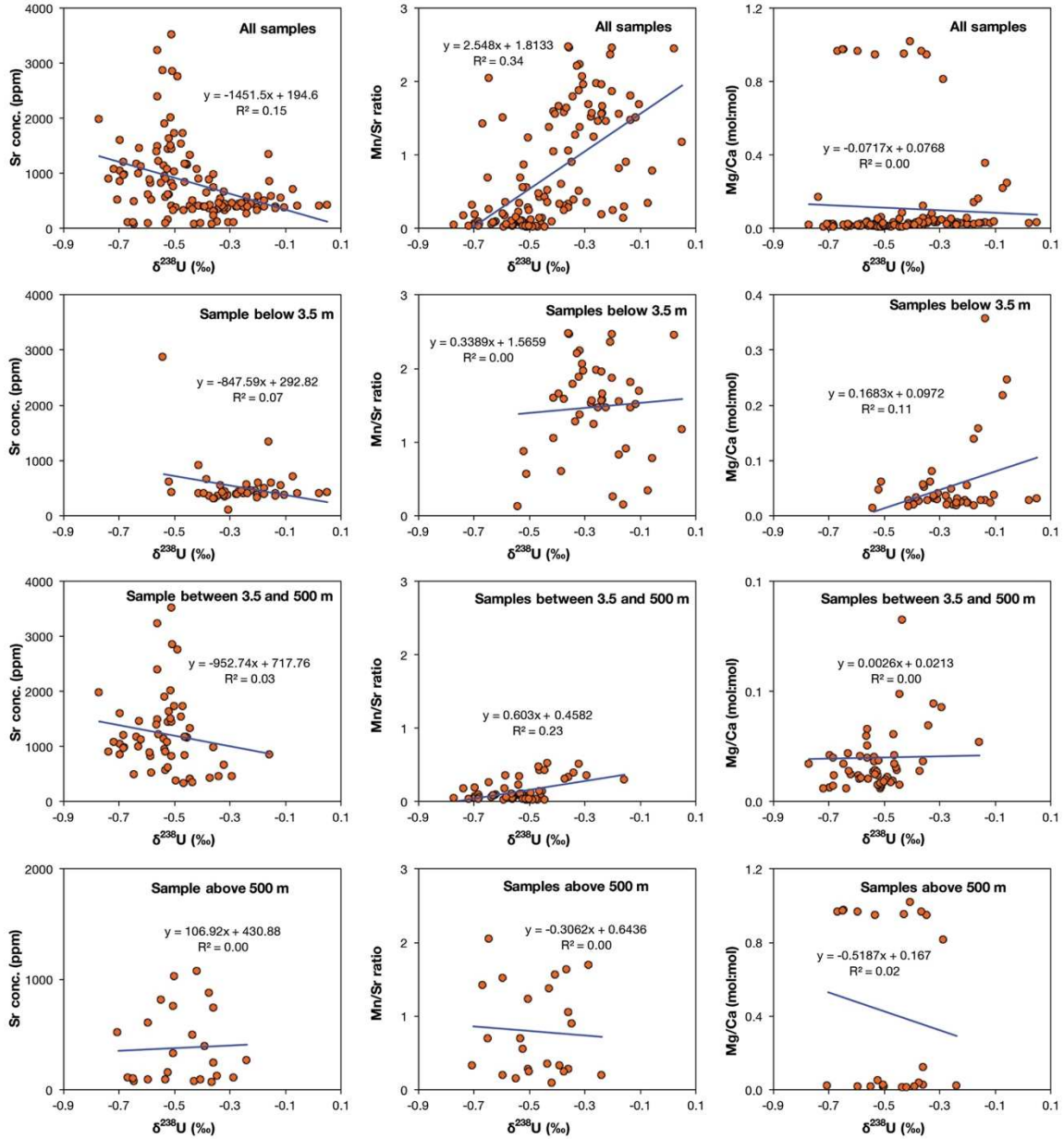
fig. S2. Diagenetic evaluation cross-plots of δ^{238}U-[Sr], δ^{238}U-Mn/Sr, and δ^{238}U-Mg/Ca (mol/mol) of all samples, samples below 3.5 m, samples between 3.5 and 500 m, and samples above 500 m.
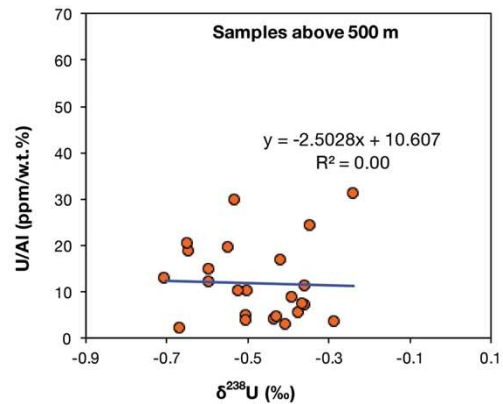
All samples
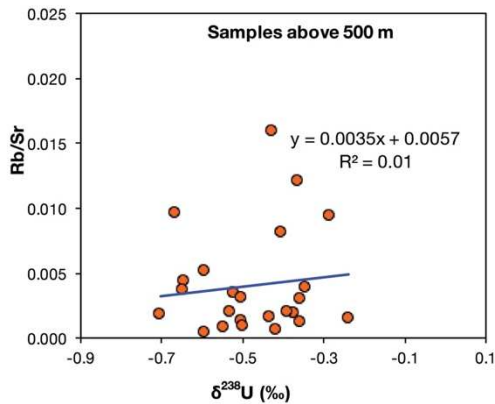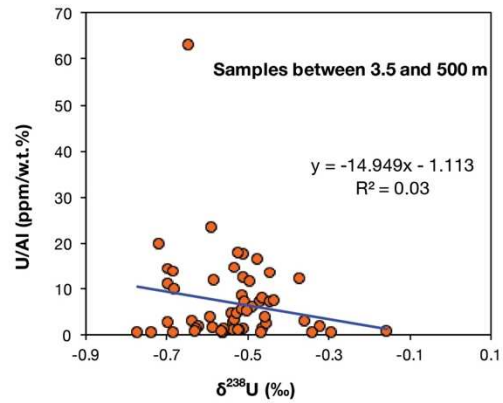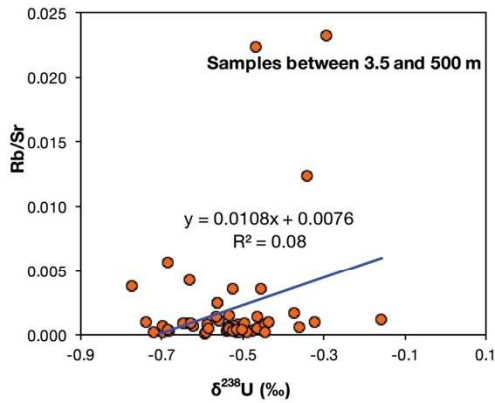$y = 0.0017x + 0.0029$
$R^2 = 0.01$

All samples
$y = -15.04x - 0.239$
$R^2 = 0.10$

Samples below 3.5 m
$y = 0.002x + 0.0021$
$R^2 = 0.05$

Samples below 3.5 m
$y = -6.342x + 0.499$
$R^2 = 0.07$

Samples between 3.5 and 500 m
$y = 0.0108x + 0.0076$
$R^2 = 0.08$

Samples between 3.5 and 500 m
$y = -14.949x - 1.113$
$R^2 = 0.03$

Samples above 500 m
$y = 0.0035x + 0.0057$
$R^2 = 0.01$

Samples above 500 m
$y = -2.5028x + 10.607$
$R^2 = 0.00$

Rb/Sr

U/Al (ppm/w.t.%)

$\delta^{238}U$ (‰)

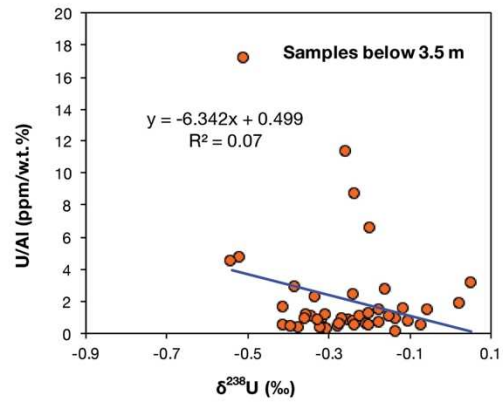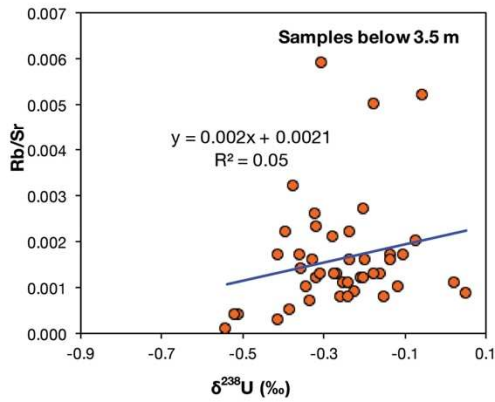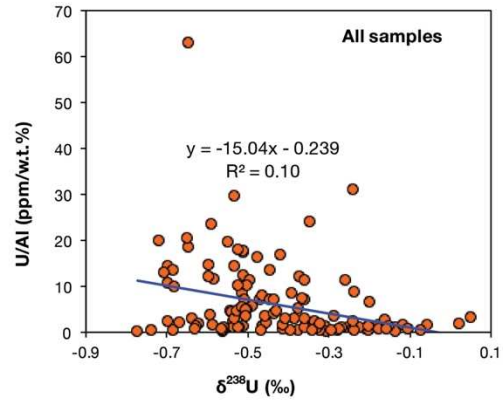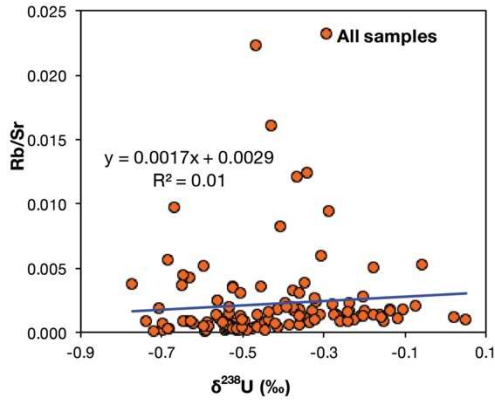**fig. S3. Cross-plots of δ^{238}U-Rb/Sr and δ^{238}U-U/Al ratio [parts per million/weight % (wt %)] for all samples and samples below and above 500 m.**

N1 event

$y = 2.3893x + 1.8781$
$R^2 = 0.28$

N1 event

$y = 0.137x + 0.088$
$R^2 = 0.17$

N1 event

$y = 0.0031x + 0.0029$
$R^2 = 0.03$

N1 event

$y = -22.969x - 3.4167$
$R^2 = 0.21$

N2 event

$y = 0.3302x + 0.2906$
$R^2 = 0.05$

N2 event

$y = -0.083x - 0.0208$
$R^2 = 0.06$

N2 event

$y = 0.0009x + 0.0024$
$R^2 = 0.00$

N2 event

$y = 22.975x + 16.704$
$R^2 = 0.22$
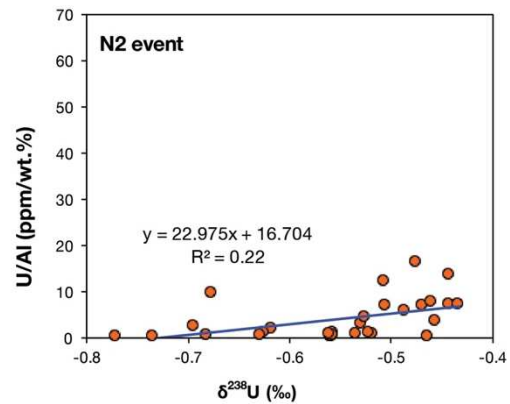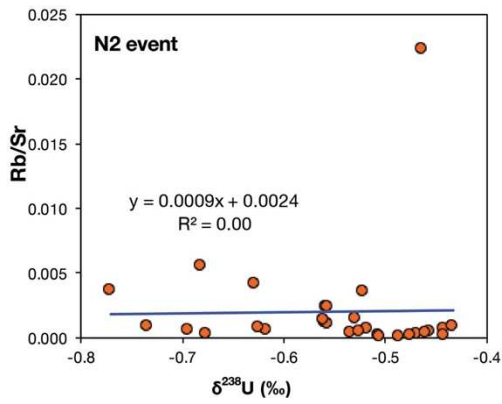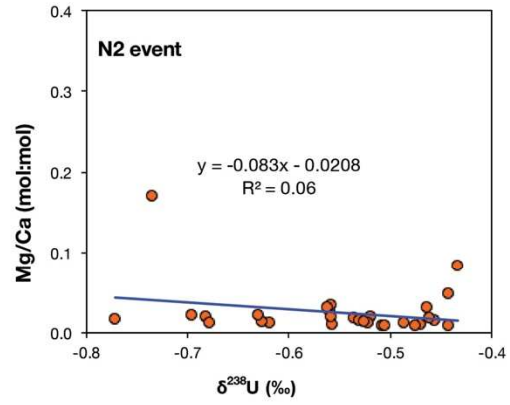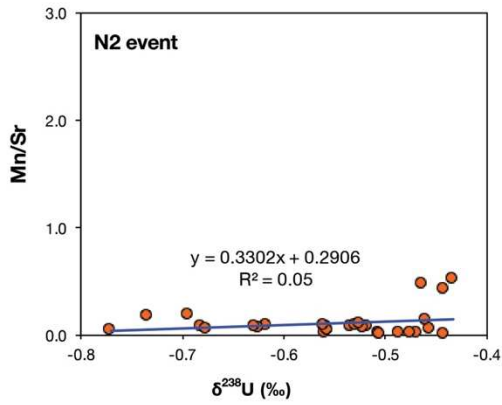
fig. S4. Cross-plots of δ^{238}U-Mn/Sr, δ^{238}U-Mg/Ca, δ^{238}U-Rb/Sr, and δ^{238}U-U/Al (wt %) for anoxic events 1 and 2. The event numbers are marked in each panel.

N3 event (Mn/Sr vs $\delta^{238}U$ (‰))
$y = 1.3919x + 0.9395$
$R^2 = 0.25$

N3 event (Mg/Ca (mol:mol) vs $\delta^{238}U$ (‰))
$y = 0.7896x + 0.4541$
$R^2 = 0.15$

N3 event (Rb/Sr vs $\delta^{238}U$ (‰))
$y = 0.0052x + 0.0038$
$R^2 = 0.23$

N3 event (U/Al (ppm/wt.%) vs $\delta^{238}U$ (‰))
$y = -7.3584x + 8.0205$
$R^2 = 0.02$

N4 event (Mn/Sr vs $\delta^{238}U$ (‰))
$y = -0.7433x + 0.9132$
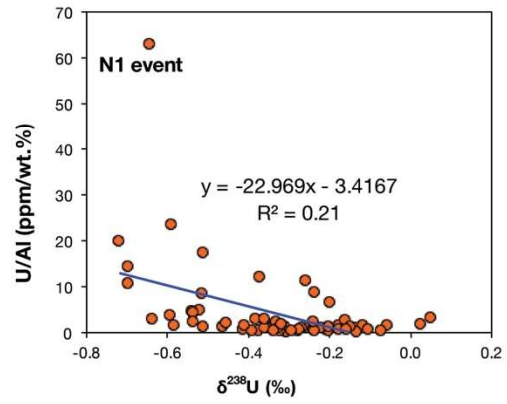$R^2 = 0.04$

N4 event (Mg/(Mg+Ca) vs $\delta^{238}U$ (‰))
$y = -1.0793x + 0.2619$
$R^2 = 0.18$

N4 event (Rb/Sr vs $\delta^{238}U$ (‰))
$y = 0.0059x + 0.0097$
$R^2 = 0.04$

N4 event (U/Al (wt.%/ppm) vs $\delta^{238}U$ (‰))
$y = -0.1335x + 12.17$
$R^2 = 0.00$
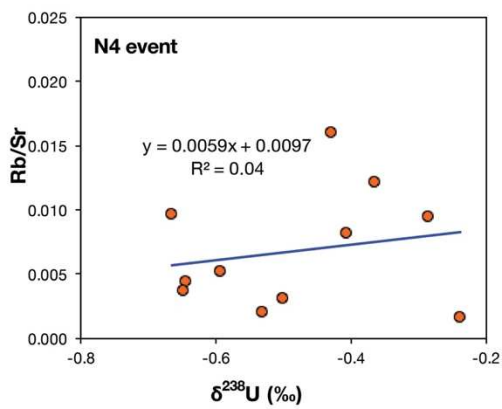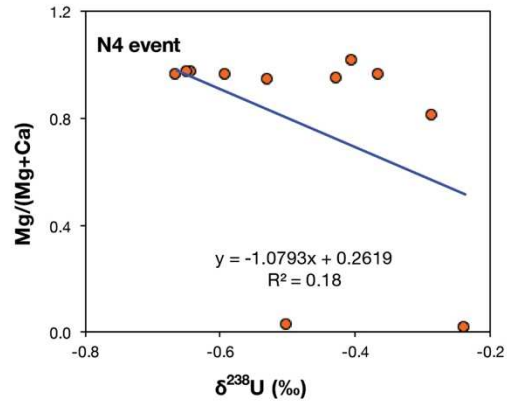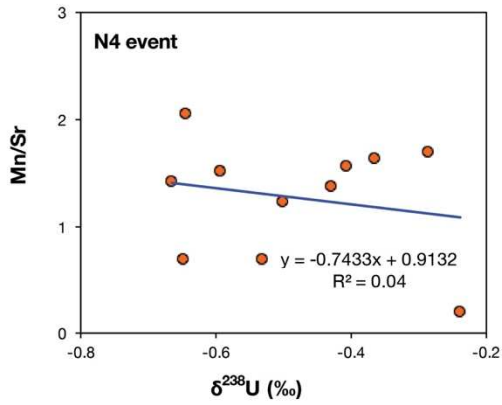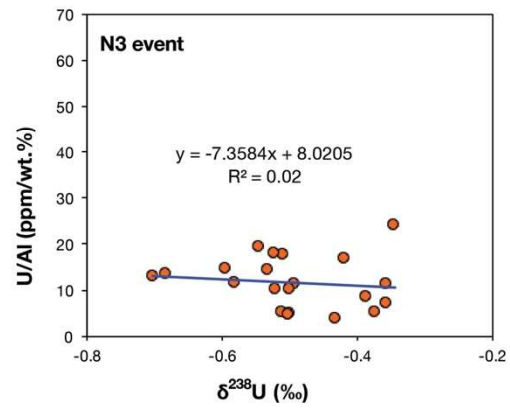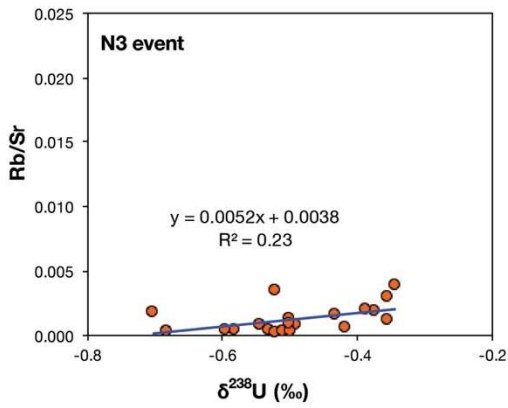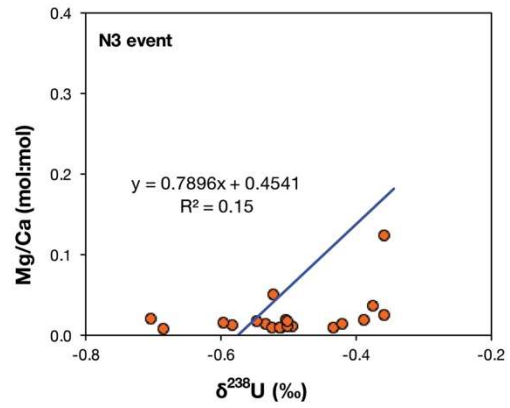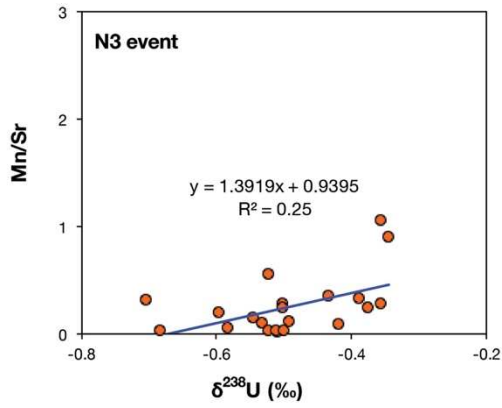
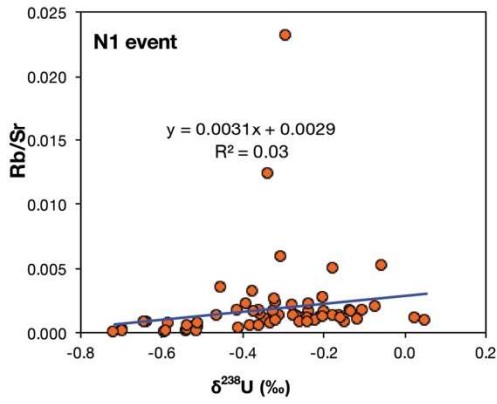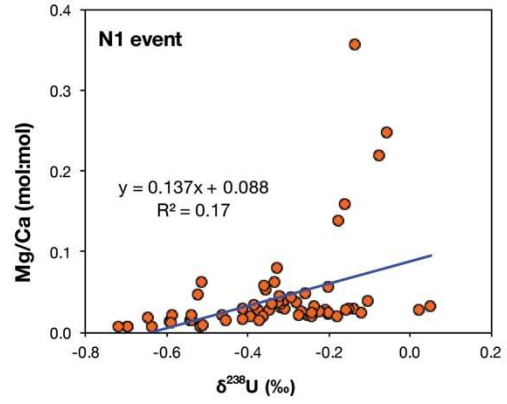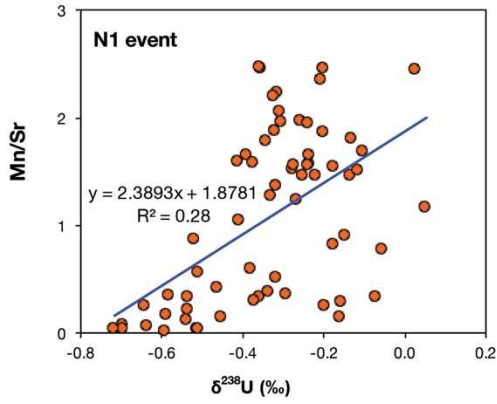**fig. S5. Cross-plots of δ^{238}U-Mn/Sr, δ^{238}U-Mg/Ca, δ^{238}U-Rb/Sr, and δ^{238}U-U/Al (wt %) for anoxic events 3 and 4.** The event numbers are marked in each panel.
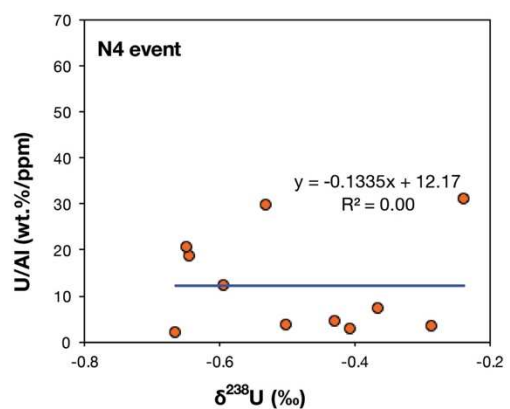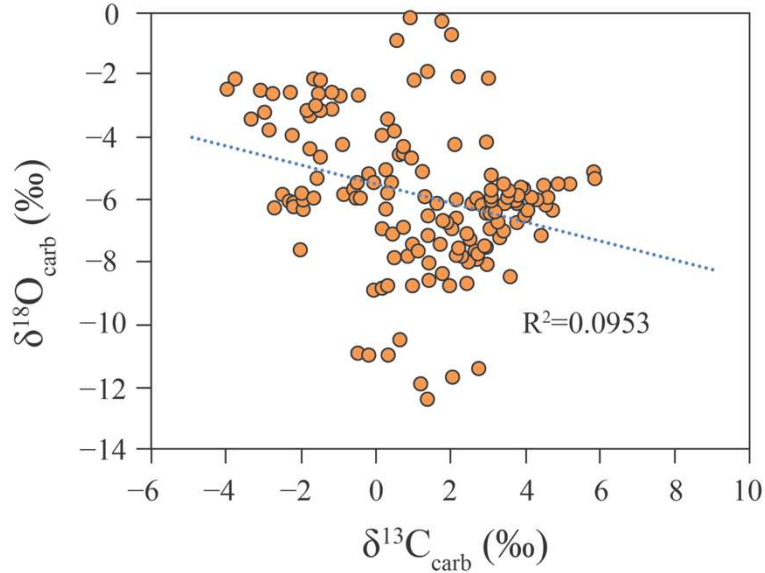
fig. S6. Cross-plots of δ^{13}C-δ^{18}O for the Zal section. In the Zal section as a whole (δ^{18}O are data from Horacek et al. (*15*)), there is no correlation between δ^{13}C and δ^{18}O ($R^2 = 0.095$).
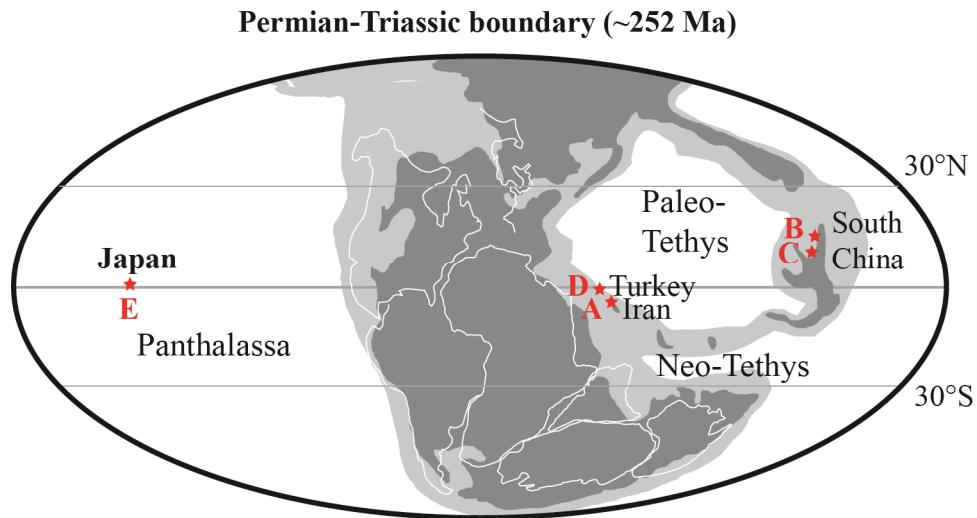
fig. S7. Location of Iran, South China, and Turkey during the Permian-Triassic transition, ~252 Ma (modified after Payne *et al*. (*60*). (A): The Zal section (Iran). (**B**) The Dawen section (South China) studied by Brennecka et al. (*22*). (**C**): The Dajiang section (South China) studied by Lau et al. (*18*). (**D**): The Taşkent section (Turkey) studied by Lau et al. (*18*). (**E**): The Kamura section (Japan) studied by Zhang et al. (*25*).
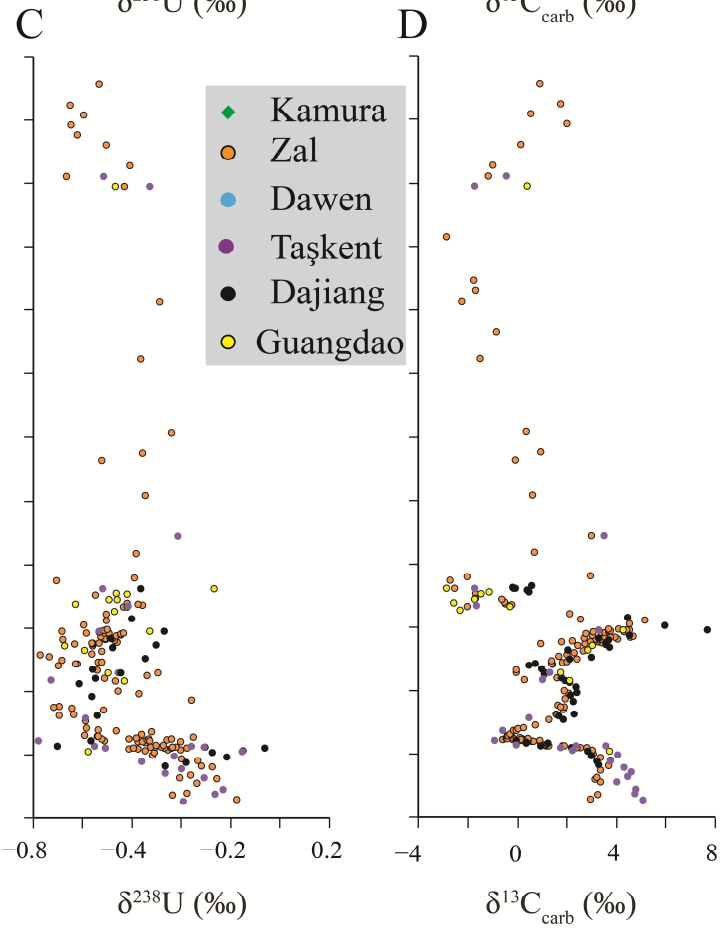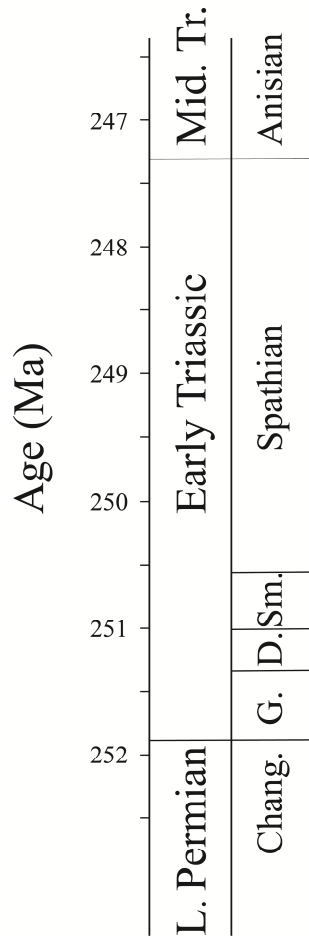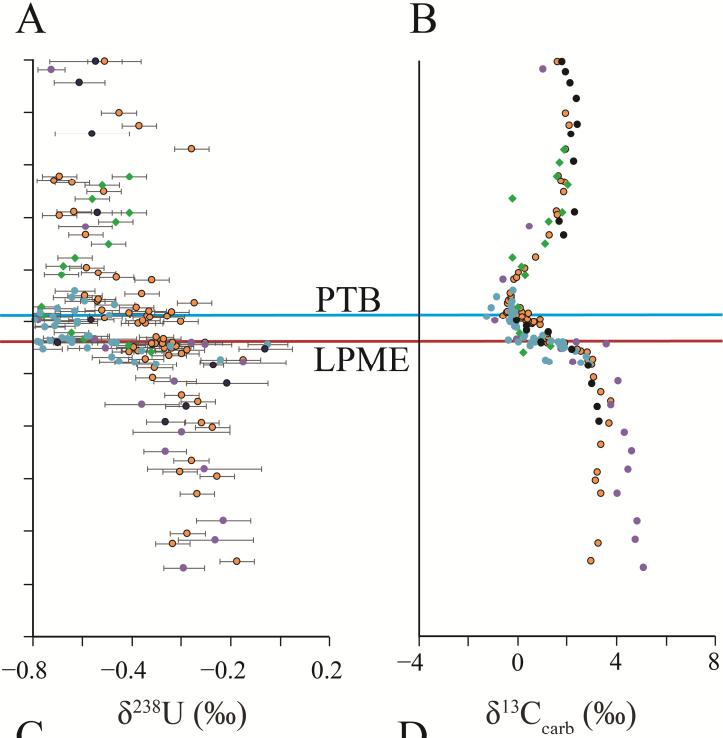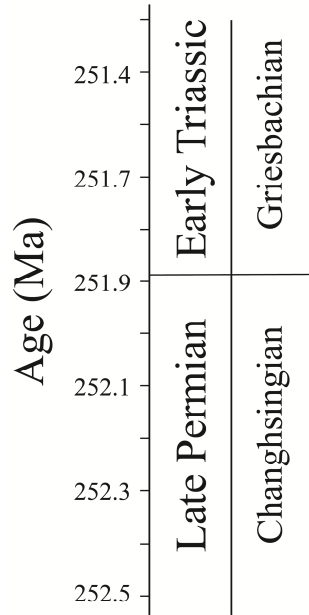
fig. S8. Comparison of U- and C-isotope profiles for Zal, Dawen, Dajiang, Taşkent, and Kamura. δ^{13}C data for Dawen are from Chen et al. (*114*), δ^{238}U data for Dawen are from Brennecka et al. (*22*)), δ^{13}C and δ^{238}U data for Dajiang and Taşkent are from Lau et al. (*18*), δ^{13}C data for Kamura are from Zhang et al. (*115*), and δ^{238}U data for Kamura are from Zhang et al. (*25*). The blue solid line denotes the Permian-Triassic boundary (PTB, 251.89 Ma), and the orange dash line denotes the latest Permian mass extinction horizon (LPME, ~251.94 Ma).
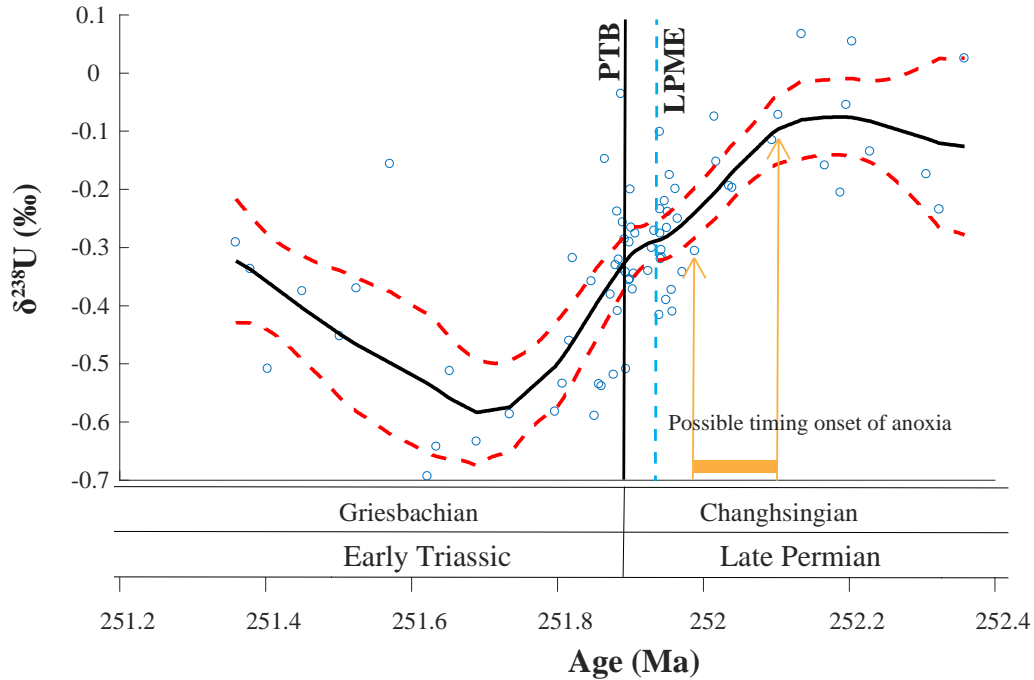
fig. S9. A LOWESS trend showing inferred timing of onset of latest Permian oceanic anoxia. Included are all $\delta^{238}U$ data in figure S8B.
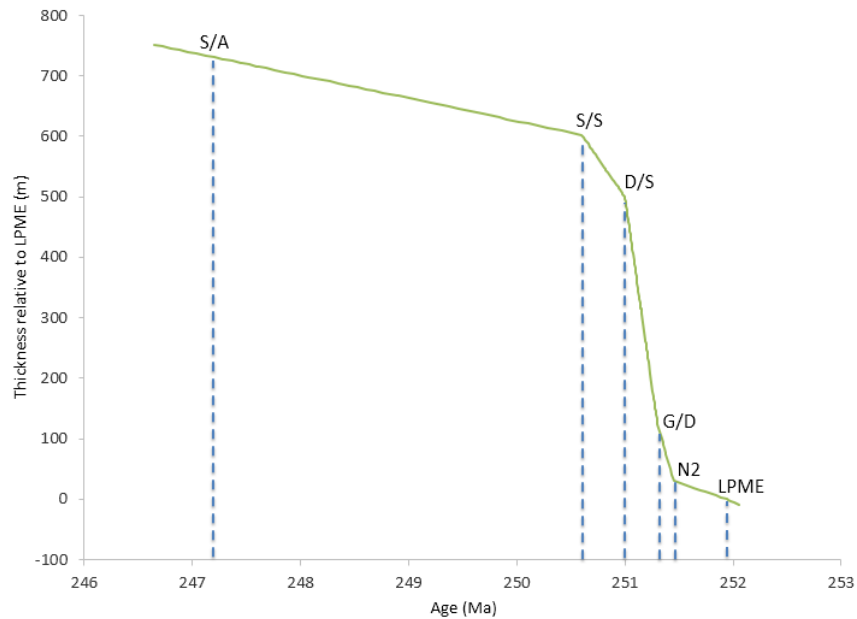
fig. S10. Age-depth model for the Zal, Iran study section. Abbreviations: LPME = latest Permian mass extinction horizon; N2 = the N2 carbon-isotope excursion; G/D = Griesbachian-Dienerian boundary; D/S = Dienerian-Smithian boundary; S/S = Smithian-Spathian boundary; S/A = Spathian-Anisian boundary.
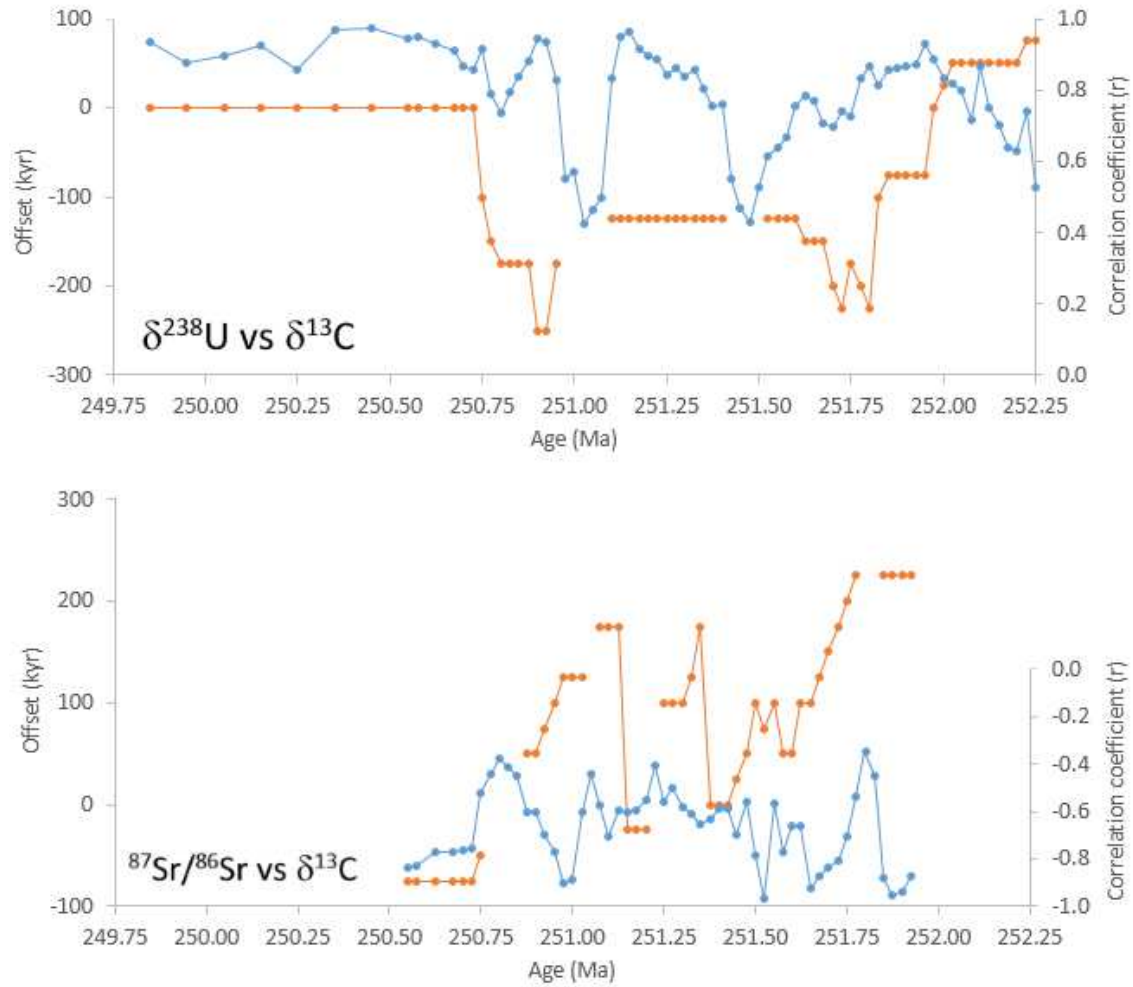
fig. S11. Cross-correlation analysis of LOWESS-smoothed curves for U-C-Sr isotope records. The orange curves represent offsets in ka (left y-axis), and the blue curves represent correlation coefficients (r; right y-axis). Gaps in the offset curves represent time windows with low correlation coefficients (r < +0.6 for U-C; r > –0.5 for Sr-C), which were characterized by less stable estimates of the offset magnitude.
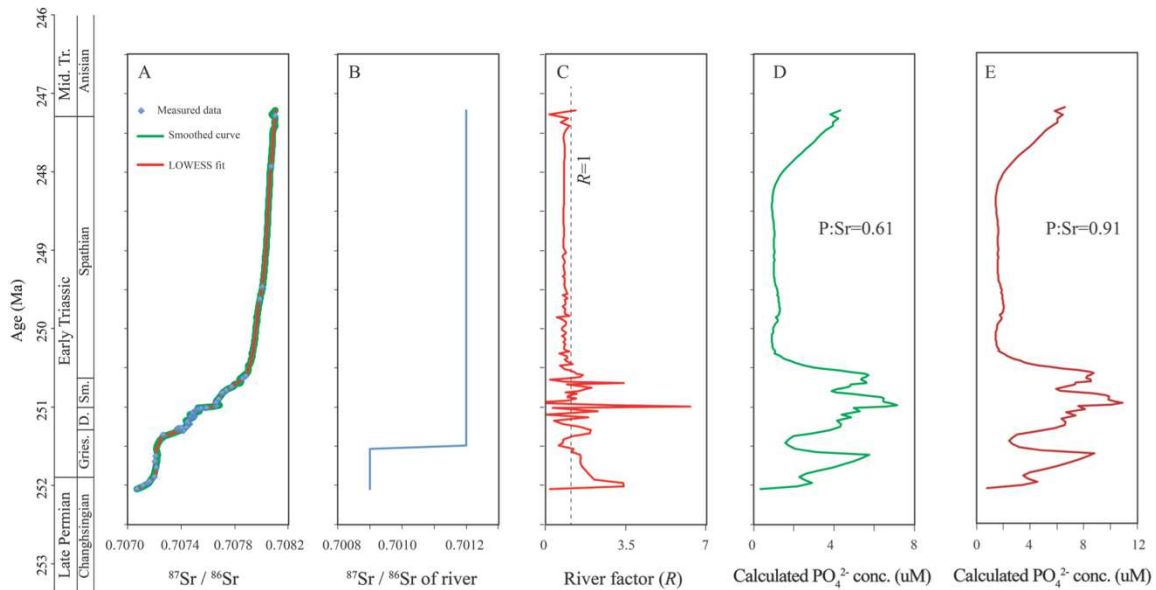
fig. S12. $^{87}Sr/^{86}Sr$ -derived estimates of the continental weathering flux and the calculated seawater PO_4^{3-} concentrations for the Early Triassic ocean. (**A**) Continental weathering fluxes, (**B**) riverine $^{87}Sr/^{86}Sr$, (**C**) "river factor" (F_R/F_M, = river flux / mantle flux), (**D**) calculated seawater PO_4^{3-} concentrations for the Early Triassic ocean assuming a P:Sr ratio of 0.61 mol:mol, and (**E**) calculated seawater PO_4^{3-} concentrations for the Early Triassic ocean assuming a P:Sr ratio of 0.91 mol:mol. In A, continental weathering fluxes were estimated based on the LOWESS trend of measured $^{87}Sr/^{86}Sr$ data (green line; from Sedlacek et al. (*38*)) and a forward model fit (red line). In B, we set riverine $^{87}Sr/^{86}Sr$ ratios for the first 0.5 Ma lower than typical average seawater values of 0.7112 because the river flux at the PTB likely contained larger amounts of Sr from weathered Siberian Traps basalts. In D and E, seawater PO_4^{3-} concentrations were estimated based on calculated riverine phosphorus inputs assuming the oceanic residence time (T') of PO_4^{3-} and the anoxic seafloor area follows a sigmoidal relationship in which T' increases when anoxic seafloor area expands.

Indian margin / Western USA / Boreal

Stage		Indian margin	Western USA	Boreal
Anisian	M			Buddhaites hagei/ Czekanowskites decipiens
Anisian	Early		Lenotropites caurus	Lenotropites caurus
Anisian	Early		Silberlingites mulleri	Lenotropites caurus
Anisian	Early		Pseudokeyserlingites guexi	Grambergia taimyrensis/ Stenopopanoceras mirabile
Anisian	Early		Japonites welteri beds	Grambergia taimyrensis/ Stenopopanoceras mirabile
Spathian			Keyserlingites subrobustus	Keyserlingites subrobustus / Olenikites spiniplicatus
Spathian			Neopopanoceras haugi	Keyserlingites subrobustus / Olenikites spiniplicatus
Spathian			Silberlingeria	Subolenekites pilaticus/ Parasibirites grambergi
Spathian			Fengshanites/Prohungarites	Subolenekites pilaticus/ Parasibirites grambergi
Spathian			Procolumbites	Subolenekites pilaticus/ Parasibirites grambergi
Spathian			Columbites parisianus	Nordophiceras contrarium
Spathian			Bajarunia confusionensis	Bajarunia euomphala
Smithian	Late	Glyptophiceras sinuatum/ Subvishnuites posterus	Anasibirites kingianus	Wasatchites tardus
Smithian	Late	Wasatchites distractus	Anasibirites kingianus	Wasatchites tardus
Smithian	Middle	Nyalamites angustecostatus	Owenites beds/ Meekoceras gracilitatis	Euflemingites romunderi/ Lepiskites kolymensis
Smithian	Middle	Pseudoceltites multiplicatus	Owenites beds/ Meekoceras gracilitatis	Euflemingites romunderi/ Lepiskites kolymensis
Smithian	Middle	Nammalites pilatoides	Owenites beds/ Meekoceras gracilitatis	Euflemingites romunderi/ Lepiskites kolymensis
Smithian	Middle	Escarguelites spitiensis	Owenites beds/ Meekoceras gracilitatis	Euflemingites romunderi/ Lepiskites kolymensis
Smithian	Middle	Brayardites compressus		Euflemingites romunderi/ Lepiskites kolymensis
Smithian	Early	Flemingites flemingianus/ Euflemingites cirratus	Flemingites beds	Euflemingites romunderi/ Lepiskites kolymensis
Smithian	Early	Rohillites rohilla	Invoites beayerensis / Preflorianites-Kashmirites beds / Meekoceras millardense / Meekoceras olivieri	Euflemingites romunderi/ Lepiskites kolymensis
Smithian	Early	Flemingites nanus/Radioceras evolvens/Vercherites cf. pulchrum	Vercherites undulatus/ Radioceras aff. evolvens	Euflemingites romunderi/ Lepiskites kolymensis
Smithian	Early	Xenodiscoides perplicatus		Hedenstroemia hedenstroemi
Smithian	Early	Shamaraites rursiradiatus/ Kashmiritidae beds		Hedenstroemia hedenstroemi
Smithian	Early	Flemingites bhargavai		Hedenstroemia hedenstroemi
Dienerian	L	Awanites awani / Koninckites vetustus / Kingites davidsonianus / Vavilovites meridialis / Ambites bjerageri/Ambites lilangensis		Hedenstroemia hedenstroemi
Dienerian	M	Ambites superior / Ambites discus / Ambites radiatus/Ambites bojeseni / Ambites atavus		V. sverdrupi/V. turgidus/K. korostelevi
Dienerian	M	Ambites superior / Ambites discus / Ambites radiatus/Ambites bojeseni / Ambites atavus		Proptychites candidus
Dienerian	E	Gyronites frequens / Gyronites plicosus / Gyronites dubius		Buekkenites strigatus/ Wordieoceras decipiens
Griesbachian				Ophiceras commune/ Tompophiceras nielseni
Griesbachian				Otoceras boreale
Griesbachian				Otoceras concavum

fig. S13. Interregional ammonoid zonation scheme. Note that some correlations are tentative. The sources on the data has been discussed in detail in section "Ammonoid extinction rates".